

PAPER

[View Article Online](#)
[View Journal](#)

Cite this: DOI: 10.1039/d0ee01538e

An aqueous hybrid electrolyte for low-temperature zinc-based energy storage devices†

Nana Chang,^{ab} Tianyu Li,^a Rui Li,^{ab} Shengnan Wang,^{ab} Yanbin Yin,^{*a} Huamin Zhang^{id}^a and Xianfeng Li^{id}^{*a}

Aqueous zinc-based energy storage (ZES) devices are promising candidates for portable and grid-scale applications owing to their intrinsically high safety, low cost, and high theoretical energy density. However, the conventional aqueous electrolytes are not capable of working at low temperature. Here we report a frigostable, cost-effective, safe and eco-friendly hybrid electrolyte with high zinc-ion conductivity (6.9 mS cm^{-1} at -40°C), and high reversibility of Zn plating/stripping, which consists of water, ethylene glycol (EG) and zinc sulfate salt (ZnSO_4). Experiments together with theoretical calculations demonstrated that the unique solvation interaction of Zn^{2+} with EG can effectively enhance the hydrogen bonding between EG and H_2O and weaken the solvation interaction of Zn^{2+} with H_2O , thus providing the hybrid electrolyte with a lower freezing point and reversible Zn/Zn^{2+} chemistry. As a proof-of-concept, both Zn-ion hybrid supercapacitors (ZHSCs) and Zn-ion batteries (ZIBs) with the hybrid electrolytes delivered high energy densities (36 W h kg^{-1} for the ZHSC and 121 W h kg^{-1} for the ZIB), high power densities (3.1 kW kg^{-1} for the ZHSC and 1.7 kW kg^{-1} for the ZIB) and long-cycle life (5500 cycles over 110 days for the ZHSC and 250 cycles for the ZIB) at -20°C . This work provides a new option for low-temperature energy storage devices.

Received 15th May 2020,
Accepted 11th August 2020

DOI: 10.1039/d0ee01538e

rsc.li/ees

Broader context

The widespread deployment of portable electronics, electric vehicles and renewable energy calls for high-performance energy storage devices. Aqueous zinc-based chemistry has received considerable interest for energy storage systems since the zinc anode features intrinsically high safety, low cost, and environmental friendliness. The main challenges in aqueous zinc-based energy storage (ZES) come from the sharply dropping ion transport at low temperatures and complex parasitic reactions related to zinc corrosion, passivation, and byproducts. In this work, we present a frigostable, cost-effective, safe and eco-friendly hybrid electrolyte consisting of water, ethylene glycol (EG) and zinc sulfate salt (ZnSO_4). A unique solvation interaction of Zn^{2+} with EG in this electrolyte can effectively enhance the hydrogen bonding between EG and H_2O and weaken the solvation interaction of Zn^{2+} with H_2O , thus providing the hybrid electrolyte with a lower freezing point and reversible Zn/Zn^{2+} chemistry at low temperature. As a result, the hybrid electrolytes enabled Zn-ion hybrid supercapacitors (ZHSCs) and Zn-ion batteries (ZIBs) with high power densities and long-cycle life at low temperature (up to -40°C) to be demonstrated. This work offers great insight to design electrolytes for low-temperature energy storage devices.

Introduction

Nowadays, the development of portable electronics, electric vehicles and renewable energy has stimulated enormous demand for high-performance energy storage devices. Lithium-ion batteries (LIBs) have the advantages of high specific energy density and energy efficiency;^{1,2} however, there are still growing concerns

over their safety,³ resource limitation,^{4,5} and cost, mainly stemming from organic electrolytes and active materials.^{6,7} Zinc-based energy storage (ZES) systems exhibit competitiveness and promise for energy storage as the zinc (Zn) anode features high theoretical capacity density (820 mA h g^{-1}), low redox potential (-0.76 V vs. standard hydrogen electrode), and abundant reserves.^{8–10} Besides, zinc-based chemistry has high compatibility with aqueous electrolytes, further endowing the system with low cost, high safety, and environmental friendliness.^{11–13}

In typical aqueous ZES, the electrolyte plays a vital role in determining the electrochemical performance since it is related to the reaction mechanism, reversibility of the zinc plating/stripping process and ionic conductivity.^{14–19} A common challenge

^a Division of Energy Storage, Dalian National Laboratory for Clean Energy, Dalian Institute of Chemical Physics, Chinese Academy of Sciences, 457 Zhongshan Road, Dalian 116023, China. E-mail: yinyanbin@dicp.ac.cn, lixianfeng@dicp.ac.cn

^b University of Chinese Academy of Sciences, Beijing 100049, China

† Electronic supplementary information (ESI) available. See DOI: 10.1039/d0ee01538e

in aqueous electrolytes of ZES comes from their notable changes in properties at low temperature, such as phase transitions, the solvation state of ions and the viscosity, which significantly decrease their electrochemical performance.^{20–25} To address this problem, several strategies have been proposed. For instance, organic solvents such as acetonitrile (AN) and dimethyl sulfoxide (DMSO) were reported^{26–29} as co-solvents to improve the properties of the electrolytes and further expand their applicable temperature range. In addition, some research efforts including highly-concentrated electrolyte^{24,30} and hydrogel electrolyte^{31–33} have attempted to improve their low-temperature performance from the perspective of lowering the freezing point (FP) of the electrolytes. Nevertheless, these viscous electrolytes inevitably induce inferior power density. Most importantly, taking the Zn-ion solvation state into account is very necessary in the design of low-temperature electrolytes; however, it has been rarely researched.

Ethylene glycol (EG) has been widely used as antifreeze in engine coolant owing to its high boiling point and relatively low FP.^{34–36} Also, EG has the characteristics of high flash point, high dielectric constant, excellent solubility in water, low cost, low volatility and fewer safety hazards as well, which render it promising as an additive in aqueous electrolytes (Table S1, ESI†). Herein, we propose a series of hybrid electrolytes with tunable FPs for low-temperature ZES. The electrolytes consist of EG, water and zinc sulfate salt (ZnSO_4) (Scheme 1a). Thanks to the unique solvation interaction of EG with Zn^{2+} , the hydrogen bonding (HB) between EG and H_2O is enhanced and thereby the HB between H_2O and H_2O is greatly broken, thus providing the hybrid electrolyte with a lowered freezing point and high ionic conductivity even at -40°C . Moreover, the FPs of the hybrid electrolytes can be well controlled by adjusting the EG-to-water ratio, which can meet different climates in various regions of China (Scheme 1b). In addition, the solvation interaction of Zn^{2+} with H_2O is partly reduced by the introduction of EG. This contributes to fewer side reactions like the hydrogen evolution reaction (HER) on the Zn anode. Interestingly, both a highly reversible zinc plating/stripping process at -20°C and more uniform zinc deposition are achieved with these hybrid electrolytes as well. Encouraged by these advantages, the versatility of the hybrid electrolytes is verified by

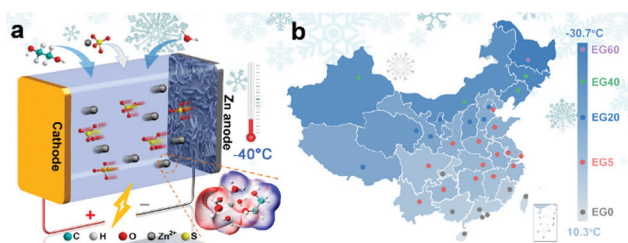
using zinc-ion hybrid supercapacitors (ZHSCs, surface adsorption/desorption reaction) and zinc-ion batteries (ZIBs, intercalation/deintercalation reaction), which demonstrate high capacity density, high power density and high cycling stability in a wide temperature range.

Results and discussion

Characterization of the hybrid electrolytes

To investigate the effect of EG on the FP of the hybrid electrolyte, a series of hybrid electrolytes with 2 M ZnSO_4 , where the EG-to-water volume ratio was raised from 0% to 5%, 20%, 40%, 60%, and 100%, were prepared. The corresponding electrolytes were marked as EG0, EG5, EG20, EG40, EG60, and EG100, respectively. As displayed in Fig. 1a, EG0 starts to freeze at -8°C , which is lower than the FP of water, which can be ascribed to the zinc salts in the aqueous solution. The FP of pure EG is measured to be -13°C , agreeing well with the reported data.³⁷ Notably, as the EG content increases, the FPs of EG5, EG20, EG40, and EG60 decrease to -11°C , -18°C , -29°C , and -33°C , respectively. The snapshots of the series of hybrid electrolytes at -20°C indicate a better anti-freezing behavior compared with “water-in-salt” electrolytes (Fig. S1, ESI†). Their ionic conductivities at various temperatures were studied by using electrochemical impedance spectroscopy (EIS) (Fig. 1b and Fig. S2, ESI†) and the values of resistances obtained from the EIS curves are displayed in Table S2 (ESI†). The increase in EG content, however, leads to a slight drop in the ionic conductivity of the hybrid electrolytes, which is probably ascribed to the gradually increasing viscosity (Fig. S3, ESI†). All ionic conductivities show a similar downward trend as the temperature decreases from 20°C to 0°C . However, when the temperature is below 0°C , all the added-EG electrolytes display much higher ionic conductivities than that of EG0. In particular, EG60 retains a high ionic conductivity of 6.90 mS cm^{-1} even at a temperature as low as -40°C , whereas the ionic conductivity of EG0 dramatically drops to 1.04 mS cm^{-1} (-40°C). As expected, the hybrid electrolytes display superior ionic conductivities over reported low-temperature electrolytes^{27,29,32,38–41} (Fig. 1c). More importantly, this series of hybrid electrolytes with tunable FPs provides a good balance between performance and cost, which enables promising application in various regions. In addition, the stable electrochemical window of the hybrid electrolyte was investigated by linear sweep voltammetry (LSV) using glassy carbon as a working electrode (Fig. S4, ESI†). A similar onset potential of the oxygen evolution reaction (OER) at 2.8 V (vs. Zn/Zn^{2+}) on the glassy carbon electrode is observed for all of the hybrid electrolytes. Notably, the subsequent OER currents of the hybrid electrolytes are greatly reduced as the EG-to-water ratio exceeds 20%, suggesting that EG can decrease the total amount of OER to some extent. Besides, the balanced EG–water proportion can not only decrease the volatility of the hybrid electrolyte effectively (Fig. S5, ESI†), but also provide a non-flammable hybrid electrolyte (Fig. S6, ESI†), further proving the practicability of this aqueous hybrid electrolyte.

To explore how EG impacts the hybrid electrolytes, we performed Fourier Transform Infrared spectroscopy (FTIR),



Scheme 1 (a) Schematic illustration of the ZES with hybrid electrolytes at low temperatures. (b) The distribution of the average lowest temperature of each province in China. The matched hybrid electrolyte has been marked in the position of the provincial capital. (Note: the weather data is the average value of the provincial capital over the past three years, which is taken from the China meteorological administration and the temperature distribution is plotted using Excel.)

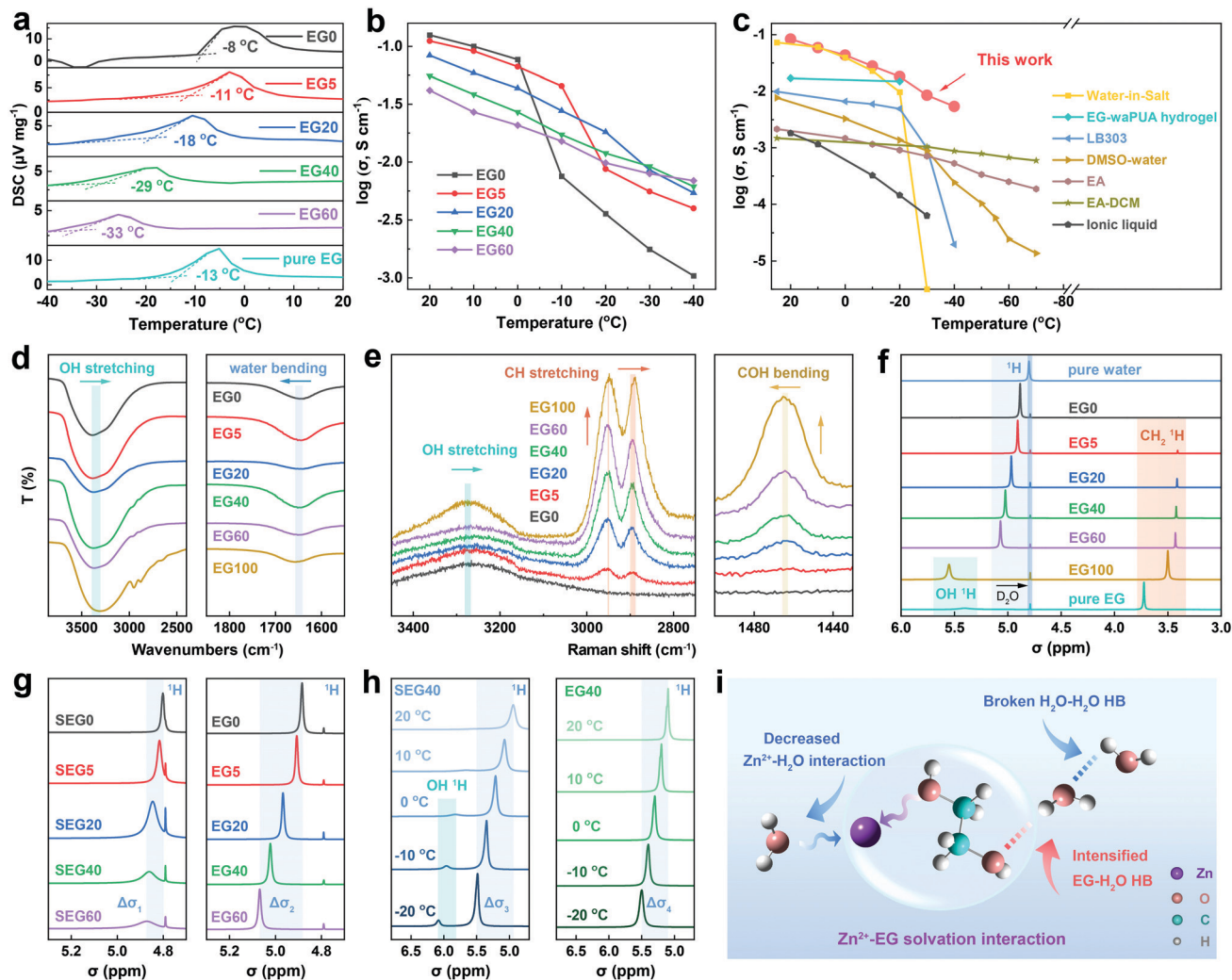


Fig. 1 Characterization of the hybrid electrolytes. (a) The FP data obtained from the differential scanning calorimetry (DSC) curves. (b) Ionic conductivities of the hybrid electrolytes at different temperatures. (c) Comparison of the hybrid electrolytes with various other low-temperature electrolytes. (d) FTIR spectrum of the hybrid electrolytes in transmission mode via CaF₂ cells. (e) Raman spectra of a series of hybrid electrolytes. (f) ¹H NMR spectrum of different electrolytes at 25 °C. Note: the constant little peak at 4.8 ppm is the residual signal of H₂O in D₂O. The ¹H resonance from OH of EG disappeared after mixing with H₂O due to hydrogen exchange.⁴⁵ (g) ¹H NMR spectrum from H₂O for EG–water hybrid solvents (SEG_x, without ZnSO₄) and added-EG hybrid electrolytes (EG_x, with ZnSO₄). (h) ¹H NMR spectrum from H₂O for SEG40 and EG40 at various temperatures. (i) Schematic illustration of a possible mechanism of how the Zn²⁺–EG solvation interaction impacts the chemistry of the hybrid electrolyte.

Raman spectroscopy, and Nuclear Magnetic Resonance (NMR). The spectral investigation results are displayed in Fig. 1d–h. The FTIR spectrum indicates an unignorable red shift in the OH stretching vibration at 3000–3500 cm^{−1} and a slight blue shift in the bending vibration of H₂O at 1600–1700 cm^{−1} as the EG content increases, implying HB between EG and H₂O^{37,42} (Fig. 1d). Also, the OH stretching (3200–3400 cm^{−1}) of H₂O in the Raman spectra shifts to lower wavenumbers with increasing EG content, verifying the HB of EG–H₂O (Fig. 1e). Besides, there is the opposite shift for COH bending (1460–1465 cm^{−1}, blue shift) and symmetric CH stretching (2890–2900 cm^{−1}, red shift) as the EG content rises. Taken together, these spectral results indicate the lower electron density of OH in H₂O and higher electron density of COH in EG, further revealing the HB interaction of EG–H₂O between the H atoms in H₂O and the

O atoms in EG. Fig. 1f–h show the ¹H NMR spectra of the hybrid electrolytes. The ¹H peak of pure water is at 4.8 ppm⁴³ (Fig. 1f) and it shifts to lower field with a larger σ value after dissolving 2 M ZnSO₄ into aqueous solution (EG0). Similarly, the ¹H resonances from OH and CH₂ of pure EG are at 5.4 ppm and 3.7 ppm,⁴⁵ respectively; however, after dissolving 2 M ZnSO₄ into EG solution (EG100), the two peaks move oppositely to 5.6 ppm and 3.5 ppm. These results indicate that the electron density of ¹H from H₂O or from OH of EG greatly decreases after dissolving ZnSO₄,⁴⁴ which convincingly proves the solvation interaction of Zn²⁺ with the O atom in both H₂O and EG molecules. This is verified by the converse shift of ¹H from CH₂ in the EG molecule. Moreover, the chemical shift of ¹H from H₂O in the hybrid electrolytes continually moves to lower field as the EG content increases and finally reaches 5.1 ppm in

EG60. It is very necessary to clarify which interaction related to EG plays a dominant role during the above movement since EG has interactions with both H_2O and Zn^{2+} . Therefore, another group of EG–water hybrid solvents without ZnSO_4 (denoted as SEG) was further studied with ^1H NMR spectroscopy for comparison (Fig. 1g). Interestingly, with the increase of the EG content for SEGx ($x = 0, 5, 20, 40, 60$), there is a slight chemical shift ($\Delta\sigma_1 = 0.07$ ppm) of ^1H from H_2O corresponding to the HB of EG– H_2O . By contrast, as the EG content rises in EGx, the chemical shift ($\Delta\sigma_2 = 0.19$ ppm) of ^1H from H_2O is much larger than $\Delta\sigma_1$, indicating stronger HB of EG– H_2O in the presence of ZnSO_4 . Because the chemical shift of ^1H from H_2O is only associated with the variable EG content, thus the intensified HB of EG– H_2O is ascribed to the solvation interaction of EG with Zn^{2+} . These results prove that the solvation interaction of EG with Zn^{2+} can significantly enhance the HB of EG– H_2O , thus enlarging the chemical shift of ^1H from H_2O (Fig. 1i). More importantly, the ^1H NMR spectra of SEG40 and EG40 (as examples) at variable temperatures were detected to investigate how the solvation interaction of EG with Zn^{2+} impacts the HB of EG– H_2O at low temperatures (Fig. 1h). As the temperature falls, the peak of H_2O in SEG40 moves to lower field and the chemical shift difference ($\Delta\sigma_3$) between -20°C and 20°C is 0.55 ppm. This phenomenon is ascribed to the ordered arrangement of solvent molecules and the strengthened HB network among solvent molecules (such as EG– H_2O and H_2O – H_2O).⁴⁶ Meanwhile, the ^1H resonance from OH of EG appears at 5.8 ppm in SEG40 when the temperature is below 0°C ,

implying that the hydrogen exchange interaction between H_2O and EG (that is the HB of EG– H_2O) weakens as the temperature decreases. This reveals that the intensified HB network for SEG40 at low temperatures mainly derives from the strengthened HB of H_2O – H_2O rather than EG– H_2O , which is exactly how water freezes.⁴⁶ In contrast, no OH ^1H resonance signal of EG is observed in EG40 at low temperatures. This implies that the HB of EG– H_2O remains unchanged at low temperatures, which is enabled by the solvation interaction of EG with Zn^{2+} as discussed earlier (Fig. 1g). Besides, $\Delta\sigma_4$ (~ 0.4 ppm) of the ^1H chemical shift in EG40 is smaller than that of SEG40, thus illustrating that the total HB network in EG40 is less than that of SEG40. Hence, the HB of H_2O – H_2O at low temperatures is easily broken by the stronger HB of EG– H_2O , significantly lowering the FP of EG40 and thereby improving its ionic conductivity at low temperatures (Fig. 1i).

To further investigate the solvation structure of the hybrid electrolytes, molecular dynamics (MD) simulations and density functional theory (DFT) calculations were performed. The statistical solvation structure of the EG0 and added-EG electrolytes was analyzed by using MD simulations (Table S3, ESI†). The corresponding radial distribution functions (RDFs) and coordination number (CN) distribution functions were then calculated (Fig. S7–S12, ESI†). The snapshots of the simulated electrolyte structure (Fig. 2a and b) reveal that the ionic solvation cluster of Zn^{2+} coordinated with SO_4^{2-} , H_2O , and EG exists in the added-EG electrolytes. The CN analysis of H_2O , EG, and SO_4^{2-} around Zn^{2+} in the series of hybrid electrolytes is

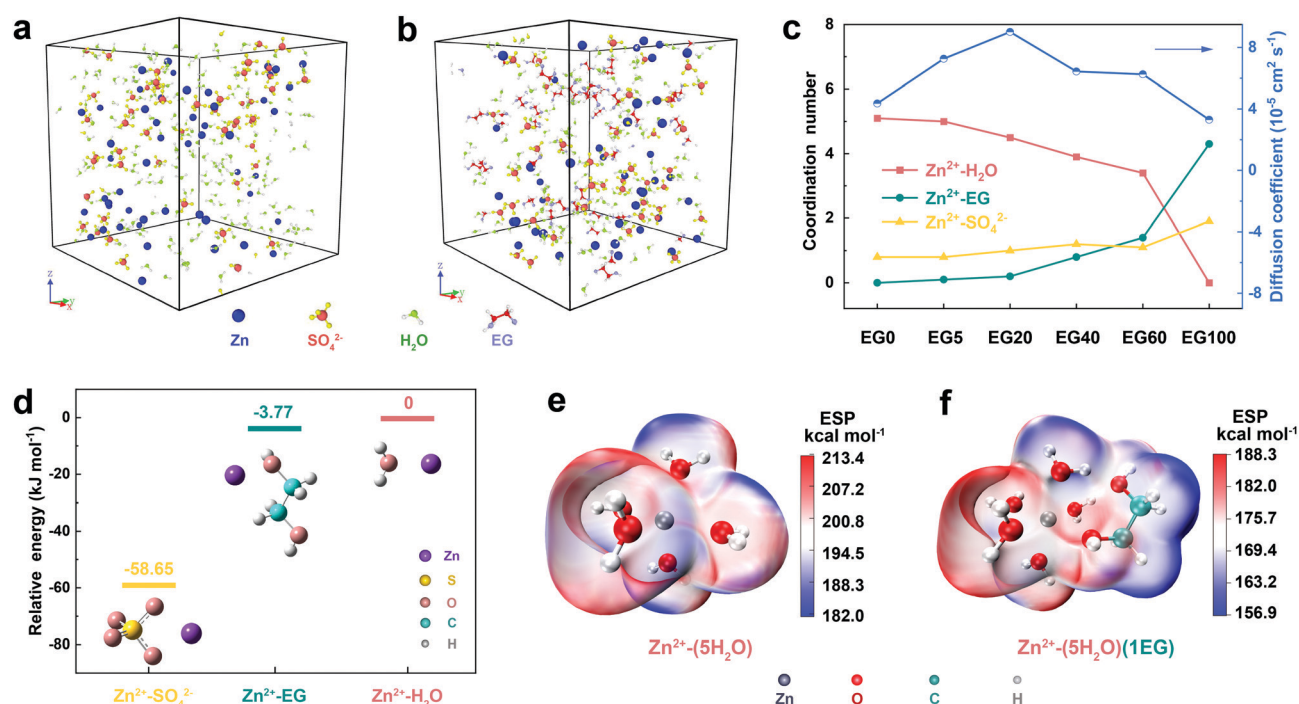


Fig. 2 Optimized structure of the hybrid electrolytes from MD simulations and DFT calculations. Snapshots of (a) EG0 and (b) EG40 during MD simulations. (c) Coordination numbers of H_2O , EG, and SO_4^{2-} around Zn^{2+} and the diffusion coefficient of Zn^{2+} in different electrolytes calculated from MD simulations. (d) Relative binding energy for Zn^{2+} with different species obtained from DFT calculations. Electrostatic potential maps of (e) the original Zn^{2+} – H_2O system and (f) the added-EG system.

displayed in Fig. 2c. With the EG-to-water ratio increasing, the CN of SO_4^{2-} anions around Zn^{2+} has a slight growth. The CN of H_2O molecules in the first hydration layer gradually decreases, whereas the CN of EG molecules increases, indicating that the introduction of EG dramatically destroys the solvation interaction of Zn^{2+} with H_2O (shown in Fig. 1i). Moreover, the diffusion rate of Zn^{2+} in these electrolytes can be qualitatively evaluated by the mean-squared displacement (MSD) as a function of time (Fig. S13, ESI†). Surprisingly, the diffusion coefficient of Zn^{2+} rises and then declines as the EG content increases (Fig. 2c). When the EG-to-water ratio is lower than 60%, the diffusion coefficient of the hybrid electrolyte is still higher than that of EG0. This result shows that the solvation structure of Zn^{2+} coordinated with EG and H_2O contributes to the fast transport of Zn^{2+} . Nevertheless, the calculated fast ion diffusion coefficient of Zn^{2+} is not quite consistent with the slight decrease in the ionic conductivities of the hybrid electrolytes at 20 °C (Fig. 1b), which probably results from the gradually increasing viscosities of the hybrid electrolytes (Fig. S3, ESI†). Even so, fast Zn-ion transport in the hybrid electrolyte is achieved at low temperatures, when the solvation interaction of EG with Zn^{2+} becomes more prominent. In addition, the relative binding energies of Zn^{2+} cations to the anion and solvent (Table S4, ESI†) can be ranked in the order of $\text{Zn}^{2+}\text{-SO}_4^{2-} > \text{Zn}^{2+}\text{-EG} > \text{Zn}^{2+}\text{-H}_2\text{O}$ (Fig. 2d). The results imply the preferential coordination of Zn^{2+} to EG rather than H_2O , resulting in the fast exchange of EG around Zn^{2+} and thereby fast conduction of Zn^{2+} in the added-EG electrolytes.^{28,29} Besides, the electrostatic potential of the $\text{Zn}^{2+}\text{-5H}_2\text{O}$ solvation state (Fig. 2e and f) has been considerably decreased after introducing EG molecules into the system. Hence, the electrostatic repulsion between Zn^{2+} cations could be decreased, which is conducive to fast Zn-ion transport.

Electrochemical reversibility and stability of Zn in the hybrid electrolytes

To explore the effects of the hybrid electrolytes on the zinc plating/stripping process, Ti||Zn half-cells were fabricated with EG0 and the hybrid electrolytes (Fig. 3a). Taking into account the FP and ionic conductivity together, EG40 with a moderate EG-to-water ratio, as an example, is employed as the electrolyte to investigate the cell performance. The deposition potential of Zn on a Ti substrate for EG40 is about 60 mV higher than that of EG0 (Fig. S14, ESI†), indicating that a more fine-grained zinc deposit can be obtained for EG40 with favorable crystallographic orientation.¹³ This could be explained by the sluggish desolvation process of EG40 since the binding energy of $\text{Zn}^{2+}\text{-EG}$ is higher than that of $\text{Zn}^{2+}\text{-H}_2\text{O}$, which is confirmed by DFT calculations (Fig. 2d). In addition, the X-ray diffraction (XRD) results (Fig. S15, ESI†) reveal that the (002) crystal plane of Zn dominates in both the EG0 and EG40 samples, implying that zinc deposits grow in directions parallel to the substrate.⁴⁷ Meanwhile, the plating/stripping potential profiles of the Ti||Zn cell with EG0 display a fluctuant and low coulombic efficiency (CE) (around 94%) (Fig. 3b and Fig. S16, ESI†) as the cycle proceeds and this cell finally fails to operate in the 60th cycle.

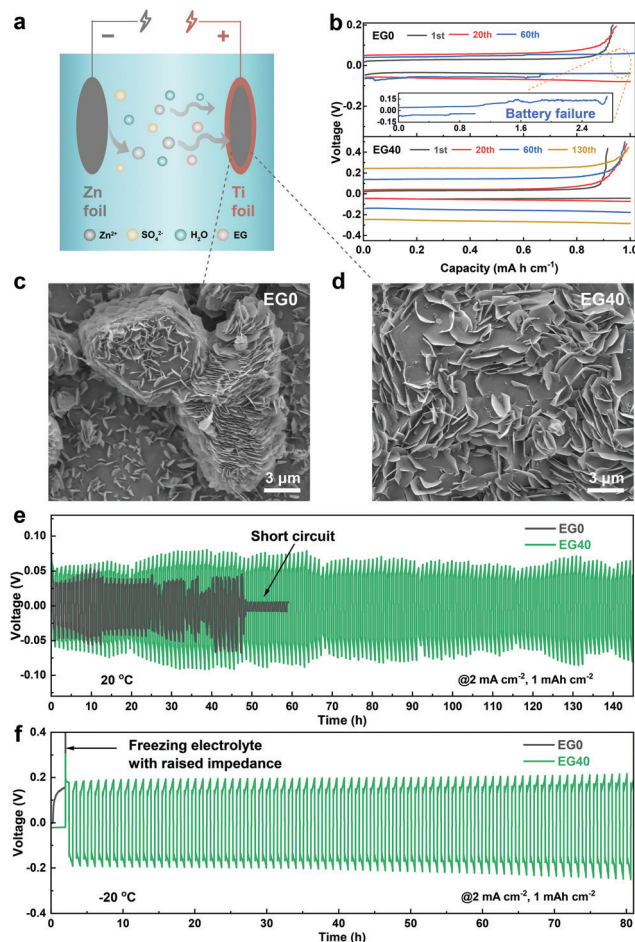


Fig. 3 Electrochemical test and physical characterization of EG0 and EG40 via Zn symmetric cells. (a) Schematic of the Ti||Zn cell. (b) Voltage profiles of Ti||Zn cells at 2 mA cm⁻². SEM images of Zn deposition on Ti foil after plating Zn with a capacity of 2 mA h cm⁻² through the Ti||Zn cells with (c) EG0 and (d) EG40. Cycling stability of Zn||Zn cells at (e) 20 °C and (f) -20 °C.

In contrast, a high and stable CE (about 98%) is achieved for the Ti||Zn cell with EG40, illustrating a highly reversible plating/stripping process enabled by the hybrid electrolytes. Moreover, the Ti||Zn cell with EG40 exhibits a persistent and higher CE of 99% at -20 °C (Fig. S17, ESI†), which indicates that the solvation interaction of Zn^{2+} with EG exerts a more prominent role in the zinc plating/stripping process especially at low temperature.

Fig. 3c and d show the SEM images of Zn deposition on Ti foil after plating Zn with a capacity of 2 mA h cm⁻² through the Ti||Zn cells. Interestingly, a uniform and dense morphology with lamellar structure is achieved for EG40. Nevertheless, the perpendicular or oblique growth of zinc deposits in EG0 leads to larger and irregular zinc particles, which are more obvious at lower magnification (Fig. S18, ESI†), which is destructive for the membrane and the whole battery stability. Therefore, the cycling stability of the Zn anode in the hybrid electrolyte was evaluated using a Zn||Zn symmetric cell under galvanostatic conditions at 20 °C (Fig. 3e) and -20 °C (Fig. 3f). At 20 °C, after cycling for 50 hours at a current density of 2 mA cm⁻², a sudden short circuit appears in the cell with EG0, resulting from the

accumulation of intensified zinc agglomeration. On the contrary, the cell with EG40 exhibits a stable polarization potential (0.05 V) over 140 hours, which benefits from dendrite-free zinc deposition. More importantly, a highly steady voltage signal for Zn/Zn²⁺ chemistry is maintained at −20 °C with EG40 (Fig. 3f). Unexpectedly, the zinc symmetric cell with EG0 cannot be operated at −20 °C owing to the sharply increased polarization in the freezing electrolyte. These results further confirm that the hybrid electrolyte promotes desirable Zn plating/stripping with high cycling stability and reversibility at low temperature.

ZES with the hybrid electrolytes

To exemplify the feasibility of the hybrid electrolytes in a real ZES system, an activated carbon cathode (AC), as a common capacitive material, was coupled with Zn to assemble ZHSCs.

The electrochemical behavior of the ZHSCs in the hybrid electrolytes was investigated by cyclic voltammetry (CV) tests (Fig. S19 and S20, ESI†). All the CV curves of the ZHSCs with the hybrid electrolytes exhibit a nearly rectangular shape and a minor redox pair at 1.2 V indicating pseudocapacitance reactions related to the stripping/plating process of Zn/Zn²⁺ (Fig. 4a).^{22,48} Meanwhile, both EG0 and EG40 exhibit capacitive-dominant behavior (Fig. 4b), which reveals the intrinsically fast kinetics of the ZHSCs.⁴⁸ Moreover, a higher capacity retention of 91.12% is observed for EG40 compared with EG0 (89.56%) after resting the battery for 24 hours, revealing the low self-discharge behavior of the ZHSC cells with the hybrid electrolytes (Fig. S21, ESI†). Fig. 4c shows the discharge capacities of the hybrid electrolytes at various temperatures at 0.1 A g^{−1}. The ZHSC with EG0 delivers a specific capacity of 73 mA h g^{−1} at

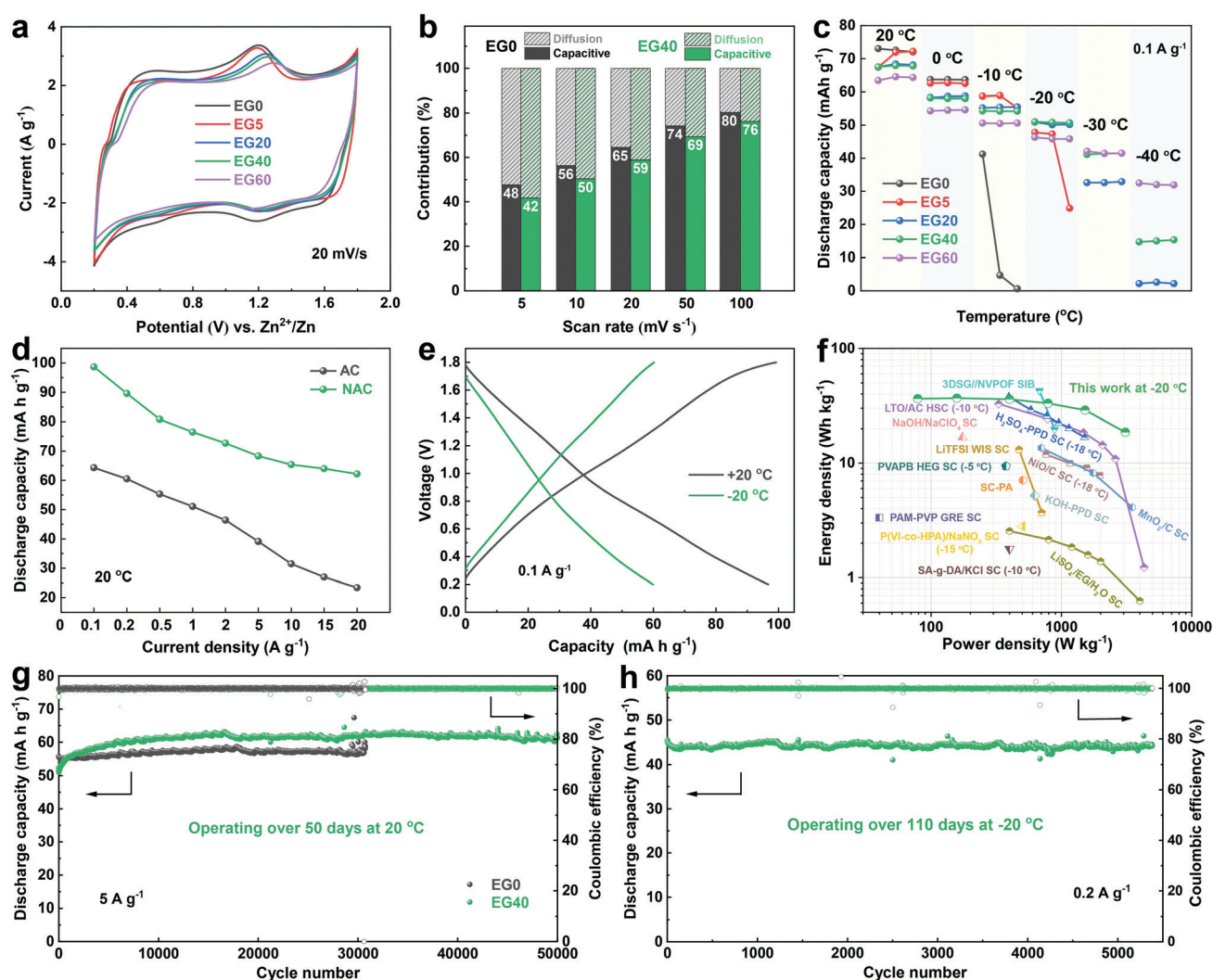


Fig. 4 Electrochemical behavior of ZHSCs. (a) CV curves of the ZHSCs with the hybrid electrolytes using the AC electrode as a working electrode and the Zn foil as the counter electrode at a scan rate of 20 mV s^{−1}. (b) The capacitive and diffusion contribution ratios to the total capacity of EG0 and EG40 at different scan rates. (c) Specific capacities at different temperature with a current density of 0.1 A g^{−1}. (d) Rate performance of AC and NAC cathodes with EG40 at various current densities ranging from 0.1 A g^{−1} to 20 A g^{−1} at 20 °C. (e) GCD profiles of ZHSCs with an NAC cathode and EG40 at 20 °C and −20 °C. (f) Ragone plot of the NAC-EG40 ZHSC in comparison to other SCs at low temperature (the temperature is −20 °C except for the special mark). (g) Cycling stability at 20 °C with a current density of 5 A g^{−1}. (h) Cycling stability for EG40 at −20 °C with a current density of 0.2 A g^{−1}.

20 °C, whereas the capacity decays dramatically when the temperature decreases to −10 °C. By contrast, the ZHSCs with hybrid electrolytes exhibit favorable low-temperature capacities. EG5 possesses superior discharge capacity than EG60 at 20 °C; however, it fails to operate below −20 °C. As the EG content increases to 40%, the ZHSCs display more than 50 mA h g^{−1} at −20 °C, which is over 75% capacity retention compared to that at 20 °C. Notably, the ZHSCs with EG60 can still maintain a high capacity retention of 50% even at −40 °C. Therefore, the low-temperature capacities of the ZHSCs with the hybrid electrolytes have been greatly improved by the fast Zn²⁺ transport at low temperature enabled by the multiple interactions of EG with Zn²⁺.

Nevertheless, limited by the deficient charge storage capacity of the commercial AC cathode, the energy densities of such ZHSC devices are still relatively low. Modifying the surface properties of commercial AC materials is an effective approach to render higher ion storage kinetics and capacity.⁴⁹ We hereby fabricate a N-doped AC (NAC) material with a superior surface area of 3124 m² g^{−1} and more pores with a size of 0.6 nm (Fig. S22, ESI[†]), which successfully improved the specific capacities, especially at high current densities (Fig. 4d). A superb energy density of 82 W h kg^{−1} is obtained for the as-prepared NAC electrode and 65% of the energy is retained at an ultrahigh power density of 15 kW kg^{−1}. Accordingly, attributed to the improved Zn²⁺ absorption/desorption of NAC and high Zn²⁺ conductivity of the hybrid electrolytes, the ZHSC with EG40 holds a very high capacity of 60 mA h g^{−1} (Fig. 4e) and competitive rate performance from 0.1 to 5 A g^{−1} at −20 °C (Fig. S23, ESI[†]). Remarkably, such a ZHSC device with EG40 delivers an outstanding energy density of 36 W h kg^{−1} and an excellent peak power density of 3.1 kW kg^{−1} at −20 °C, which is significantly superior to those of carbon-based hybrid devices^{24,50–63} (Fig. 4f and Fig. S24, ESI[†]). Moreover, extremely extraordinary cycling durability is achieved for EG40, which continuously runs over 50 000 cycles (~50 days) without noticeable capacity decay (Fig. 4g). Unfortunately, the ZHSC with EG0 displays a fluctuant capacity after 30 000 cycles, mainly stemming from the unstable operation process caused by accumulated zinc particles. To further reveal how EG impacts the interfacial reaction on the cathode side in the hybrid electrolytes, the surfaces of AC cathodes before and after charge–discharge cycles with EG0 and EG40 were investigated by XRD and SEM (Fig. S25 and S26, ESI[†]). According to previous research, the byproduct of Zn₄SO₄(OH)₆H₂O (JCPDS#39-0690) on an AC cathode is ascribed to the increased pH of the electrolyte caused by the HER on the anode side. Interestingly, the weaker peak of Zn₄SO₄(OH)₆H₂O in the XRD patterns and less sheet-like products in the SEM images further explain why EG40 improves the cycling performance of the ZHSC cell. In addition, EG40 endows the ZHSC with ultralong-term and steady operation over 110 days with a current density of 0.2 A g^{−1} at −20 °C (Fig. 4h) and considerable cycling stability at 2 A g^{−1} under −20 °C (Fig. S27, ESI[†]). As a result, the excellent Zn²⁺ adsorption/desorption behavior on the NAC cathode and fast Zn²⁺ transport in the hybrid electrolytes endow the ZHSCs with remarkable charge/discharge capability at various temperatures.

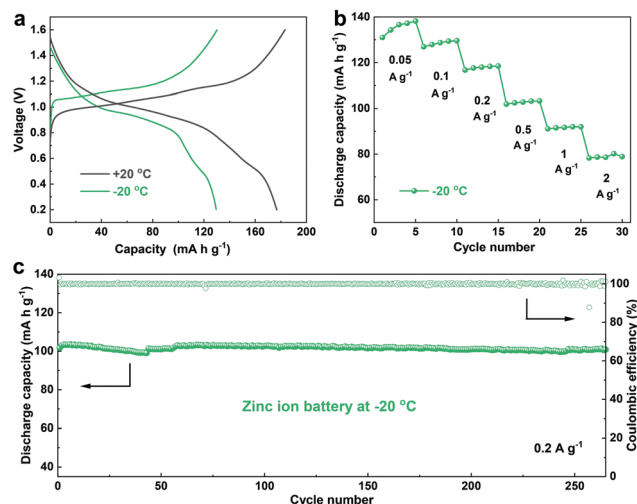


Fig. 5 Low-temperature performance of Zn//PANI-V₂O₅ batteries based on EG40. (a) GCD profiles at 20 °C and −20 °C with a current density of 0.1 A g^{−1}. (b) Rate performance of EG40 at −20 °C with various current densities ranging from 0.05 A g^{−1} to 2 A g^{−1}. (c) Cycling stability of EG40 at −20 °C with a current density of 0.2 A g^{−1}.

To demonstrate the versatility of the hybrid electrolytes in the ZES system, we further assembled ZIBs by employing PANI-intercalated V₂O₅ composites as a cathode and Zn foil as an anode. The cycling stability of the Zn//PANI-V₂O₅ battery with EG40 at room temperature is obviously improved compared to EG0 (Fig. S28, ESI[†]), which probably results from combined effects including the decreased interfacial reaction on the cathode side and flat zinc deposition on the anode side. Particularly, the Zn//PANI-V₂O₅ battery with EG40 presents a high capacity of 180 mA h g^{−1} at 20 °C and still retains an admirable capacity of 130 mA h g^{−1} at −20 °C (Fig. 5a). Besides, a fascinating rate performance at 0.05–2 A g^{−1} was achieved at such a low temperature (Fig. 5b). Additionally, the charge/discharge cycling test proves that a high discharge capacity of 100 mA h g^{−1} and a stable CE of nearly 100% are maintained over 250 cycles at −20 °C (Fig. 5c). These results confirm that the enhanced Zn²⁺ conductivity in hybrid electrolytes can not only boost the Zn²⁺-absorption/desorption process, but also promote the Zn²⁺-intercalation/deintercalation process. Therefore, the mechanism of the exceptional Zn²⁺ transport provided by the multiple solvation interactions of Zn²⁺ with the EG–water co-solvent displays generality for various cathode materials, which offers a promising solution for low-temperature aqueous ZES systems.

Conclusions

In summary, a frigestable, cost-effective, and high-Zn²⁺ conductivity EG–water hybrid electrolyte is proposed and applied in low-temperature ZES. Owing to the intensified HB of EG–H₂O and weakened solvation interaction of Zn²⁺ with H₂O enabled by the solvation interaction of EG with Zn²⁺, this hybrid electrolyte demonstrated a high Zn²⁺ conductivity and

reversibility even at temperatures as low as $-40\text{ }^{\circ}\text{C}$ and thereby enabled ZES devices to operate well in a wide range of temperatures from $20\text{ }^{\circ}\text{C}$ to $-40\text{ }^{\circ}\text{C}$. As a proof-of-concept, the ZHSCs assembled with a homemade NAC cathode in the hybrid electrolytes deliver a superb energy density of 36 W h kg^{-1} and a high-power density of 3.1 kW kg^{-1} , together with remarkable long-term cycling durability over 5000 cycles (more than 110 days) at $-20\text{ }^{\circ}\text{C}$. Moreover, when assembled with a vanadium oxide cathode, the ZIBs with the hybrid electrolytes also exhibit outstanding performance with an energy density of 121 W h kg^{-1} and power density of 1.7 kW kg^{-1} at $-20\text{ }^{\circ}\text{C}$. This work not only proposes a high-safety, low-cost, and eco-friendly hybrid electrolyte with fast Zn^{2+} transport for all-climate ZES devices, but also shows insight into the solvation structure of Zn^{2+} in the hybrid electrolytes, which provides new ideas in designing low-temperature electrolytes.

Conflicts of interest

The authors declare no conflict of interest.

Acknowledgements

This work was financially supported by the National Natural Science Foundation of China (Grant No. 21935003, 21908217 and 51677176), DICP&QIBEBT (UN201707), the China Postdoctoral Science Foundation (No. 2019M651158) and CAS Engineering Laboratory for Electrochemical Energy Storage. The authors would like to thank Prof. Xuanjun Ai (Division of Energy Research Resources) and Fan Li (Solid-state NMR & Catalytic Chemistry Group) for the NMR test.

Notes and references

- 1 A. Manthiram, X. Yu and S. Wang, *Nat. Rev. Mater.*, 2017, **2**, 1–16.
- 2 J. Liang, X. Li, Y. Zhao, L. V. Goncharova, G. Wang, K. R. Adair, C. Wang, R. Li, Y. Zhu, Y. Qian, L. Zhang, R. Yang, S. Lu and X. Sun, *Adv. Mater.*, 2018, **30**, 1804684.
- 3 M. Jacoby, *Chem. Eng. News*, 2013, **91**, 33–37.
- 4 T. C. Wanger, *Conserv. Lett.*, 2011, **4**, 202–206.
- 5 N. Wang, Y. Wang, Z. Bai, Z. Fang, X. Zhang, Z. Xu, Y. Ding, X. Xu, Y. Du, S. Dou and G. Yu, *Energy Environ. Sci.*, 2020, **13**, 562–570.
- 6 J. M. Tarascon and M. Armand, *Nature*, 2001, **414**, 359–367.
- 7 Z. Liang, Y. Zhou and Y.-C. Lu, *Energy Environ. Sci.*, 2018, **11**, 3500–3510.
- 8 A. Naveed, H. Yang, Y. Shao, J. Yang, N. Yanna, J. Liu, S. Shi, L. Zhang, A. Ye, B. He and J. Wang, *Adv. Mater.*, 2019, **31**, e1900668.
- 9 B. Tang, L. Shan, S. Liang and J. Zhou, *Energy Environ. Sci.*, 2019, **12**, 3288–3304.
- 10 H. Jia, Z. Wang, B. Tawiah, Y. Wang, C.-Y. Chan, B. Fei and F. Pan, *Nano Energy*, 2020, **70**, 104523.
- 11 J. Huang, Z. Guo, Y. Ma, D. Bin, Y. Wang and Y. Xia, *Small Methods*, 2019, **3**, 1800272.
- 12 S. Huang, J. Zhu, J. Tian and Z. Niu, *Chemistry*, 2019, **25**, 14480–14494.
- 13 Z. Zhao, J. Zhao, Z. Hu, J. Li, J. Li, Y. Zhang, C. Wang and G. Cui, *Energy Environ. Sci.*, 2019, **12**, 1938–1949.
- 14 Y. Wang, C. Wang, Z. Ni, Y. Gu, B. Wang, Z. Guo, Z. Wang, D. Bin, J. Ma and Y. Wang, *Adv. Mater.*, 2020, **32**, 2000338.
- 15 S. D. Han, N. N. Rajput, X. Qu, B. Pan, M. He, M. S. Ferrandon, C. Liao, K. A. Persson and A. K. Burrell, *ACS Appl. Mater. Interfaces*, 2016, **8**, 3021–3031.
- 16 P. Senguttuvan, S.-D. Han, S. Kim, A. L. Lipson, S. Tepavcevic, T. T. Fister, I. D. Bloom, A. K. Burrell and C. S. Johnson, *Adv. Energy Mater.*, 2016, **6**, 1600826.
- 17 N. Zhang, F. Cheng, Y. Liu, Q. Zhao, K. Lei, C. Chen, X. Liu and J. Chen, *J. Am. Chem. Soc.*, 2016, **138**, 12894–12901.
- 18 Z. Wang, J. Huang, Z. Guo, X. Dong, Y. Liu, Y. Wang and Y. Xia, *Joule*, 2019, **3**, 1289–1300.
- 19 D. W. McOwen, D. M. Seo, O. Borodin, J. Vatamanu, P. D. Boyle and W. A. Henderson, *Energy Environ. Sci.*, 2014, **7**, 416–426.
- 20 S. S. Zhang, K. Xu and T. R. Jow, *Electrochim. Acta*, 2004, **49**, 1057–1061.
- 21 X. Zang, R. Zhang, Z. Zhen, W. Lai, C. Yang, F. Kang and H. Zhu, *Nano Energy*, 2017, **40**, 224–232.
- 22 H. Zhou, C. Liu, J.-C. Wu, M. Liu, D. Zhang, H. Song, X. Zhang, H. Gao, J. Yang and D. Chen, *J. Mater. Chem. A*, 2019, **7**, 9708–9715.
- 23 H. Gao, Z. Zhao, Y. Cai, J. Zhou, W. Hua, L. Chen, L. Wang, J. Zhang, D. Han, M. Liu and L. Jiang, *Nat. Commun.*, 2017, **8**, 15911.
- 24 T. Deng, W. Zhang, H. Zhang and W. Zheng, *Energy Technol.*, 2018, **6**, 605–612.
- 25 A. Hollas, X. Wei, V. Murugesan, Z. Nie, B. Li, D. Reed, J. Liu, V. Sprenkle and W. Wang, *Nat. Energy*, 2018, **3**, 508–514.
- 26 Q. Dou, S. Lei, D.-W. Wang, Q. Zhang, D. Xiao, H. Guo, A. Wang, H. Yang, Y. Li, S. Shi and X. Yan, *Energy Environ. Sci.*, 2018, **11**, 3212–3219.
- 27 Q. Nian, J. Wang, S. Liu, T. Sun, S. Zheng, Y. Zhang, Z. Tao and J. Chen, *Angew. Chem., Int. Ed.*, 2019, **131**, 17150–17155.
- 28 J. Chen, J. Vatamanu, L. Xing, O. Borodin, H. Chen, X. Guan, X. Liu, K. Xu and W. Li, *Adv. Energy Mater.*, 2019, **10**, 1902654.
- 29 X. Dong, Y. Lin, P. Li, Y. Ma, J. Huang, D. Bin, Y. Wang, Y. Qi and Y. Xia, *Angew. Chem., Int. Ed.*, 2019, **131**, 5679–5683.
- 30 X. Dong, H. Yu, Y. Ma, J. L. Bao, D. G. Truhlar, Y. Wang and Y. Xia, *Chemistry*, 2017, **23**, 2560–2565.
- 31 Q. Rong, W. Lei, L. Chen, Y. Yin, J. Zhou and M. Liu, *Angew. Chem., Int. Ed.*, 2017, **56**, 14159–14163.
- 32 F. Mo, G. Liang, Q. Meng, Z. Liu, H. Li, J. Fan and C. Zhi, *Energy Environ. Sci.*, 2019, **12**, 706–715.
- 33 X. Jin, G. Sun, G. Zhang, H. Yang, Y. Xiao, J. Gao, Z. Zhang and L. Qu, *Nano Res.*, 2019, **12**, 1199–1206.
- 34 A. Tron, S. Jeong, Y. D. Park and J. Mun, *ACS Sustain. Chem. Eng.*, 2019, **7**, 14531–14538.
- 35 S. M. Peyghambarzadeh, S. H. Hashemabadi, S. M. Hoseini and M. Seifi Jamnani, *Int. Commun. Heat Mass Transfer*, 2011, **38**, 1283–1290.

- 36 C. Ramasamy, J. Palma del Val and M. Anderson, *J. Power Sources*, 2014, **248**, 370–377.
- 37 R. M. Kumar, P. Baskar, K. Balamurugan, S. Das and V. Subramanian, *J. Phys. Chem. A*, 2012, **116**, 4239–4247.
- 38 X. Dong, Z. Guo, Z. Guo, Y. Wang and Y. Xia, *Joule*, 2018, **2**, 902–913.
- 39 E. Iwama, P. L. Taberna, P. Azais, L. Brégeon and P. Simon, *J. Power Sources*, 2012, **219**, 235–239.
- 40 L. Jiang, Y. Lu, C. Zhao, L. Liu, J. Zhang, Q. Zhang, X. Shen, J. Zhao, X. Yu, H. Li, X. Huang, L. Chen and Y.-S. Hu, *Nat. Energy*, 2019, **4**, 495–503.
- 41 A. Eftekhari, *Energy Storage Mater.*, 2017, **9**, 47–69.
- 42 J. Zhang, P. Zhang, K. Ma, F. Han, G. Chen and X. Wei, *Sci. China, Ser. B: Chem.*, 2008, **51**, 420–426.
- 43 Y. C. Ning, *Interpretation of Organic Spectra*, John Wiley & Sons (Asia) Pte. Ltd, Singapore, 2011.
- 44 J. S. Lomas, L. Joubert and F. Maurel, *Magn. Reson. Chem.*, 2016, **54**, 805–814.
- 45 K. A. Petterson, R. S. Stein, M. D. Drake and J. D. Roberts, *Magn. Reson. Chem.*, 2005, **43**, 225–230.
- 46 J. Steele, J. Ames and M. P. Augustine, *Magn. Reson. Chem.*, 2020, **58**, 163–169.
- 47 J. Zheng, Q. Zhao, T. Tang, J. Yin, C. D. Quilty, G. D. Renderos, X. Liu, Y. Deng, L. Wang, D. C. Bock, C. Jaye, D. Zhang, E. S. Takeuchi, K. J. Takeuchi, A. C. Marschilok and L. A. Archer, *Science*, 2019, **366**, 645–648.
- 48 Y. Lu, Z. Li, Z. Bai, H. Mi, C. Ji, H. Pang, C. Yu and J. Qiu, *Nano Energy*, 2019, **66**, 104132.
- 49 H. Zhang, Q. Liu, Y. Fang, C. Teng, X. Liu, P. Fang, Y. Tong and X. Lu, *Adv. Mater.*, 2019, **31**, e1904948.
- 50 M. Wang, L. Fan, G. Qin, X. Hu, Y. Wang, C. Wang, J. Yang and Q. Chen, *J. Membr. Sci.*, 2020, **597**, 117740.
- 51 H. Shim, Ö. Budak, V. Haug, M. Widmaier and V. Presser, *Electrochim. Acta*, 2020, **337**, 135760.
- 52 S.-W. Xu, M.-C. Zhang, G.-Q. Zhang, J.-H. Liu, X.-Z. Liu, X. Zhang, D.-D. Zhao, C.-L. Xu and Y.-Q. Zhao, *J. Power Sources*, 2019, **441**, 227220.
- 53 Y.-Y. Wang, B.-H. Hou, J.-Z. Guo, Q.-L. Ning, W.-L. Pang, J. Wang, C.-L. Lü and X.-L. Wu, *Adv. Energy Mater.*, 2018, **8**, 1703252.
- 54 W. Lv, R. Xue, S. Chen and M. Jiang, *Chin. Chem. Lett.*, 2018, **29**, 637–640.
- 55 J. Wang, F. Liu, F. Tao and Q. Pan, *ACS Appl. Mater. Interfaces*, 2017, **9**, 27745–27753.
- 56 F. Tao, L. Qin, Z. Wang and Q. Pan, *ACS Appl. Mater. Interfaces*, 2017, **9**, 15541–15548.
- 57 L. Su, L. Gong, C. Ma, X. Wang and Z. Sun, *ChemElectroChem*, 2017, **4**, 46–48.
- 58 X. Li, L. Liu, X. Wang, Y. S. Ok, J. A. W. Elliott, S. X. Chang and H. J. Chung, *Sci. Rep.*, 2017, **7**, 1685–1695.
- 59 L. Su, L. Gong, X. Wang and H. Pan, *Int. J. Energy Res.*, 2016, **40**, 763–769.
- 60 R. Vellacheri, A. Al-Haddad, H. Zhao, W. Wang, C. Wang and Y. Lei, *Nano Energy*, 2014, **8**, 231–237.
- 61 L. Su, L. Gong, H. Lü and Q. Xü, *J. Power Sources*, 2014, **248**, 212–217.
- 62 A. J. Roberts, A. F. Danil de Namor and R. C. Slade, *Phys. Chem. Chem. Phys.*, 2013, **15**, 3518–3526.
- 63 Z.-D. Huang, A. Chen, F.-N. Mo, G.-J. Liang, X.-L. Li, Q. Yang, Y. Guo, Z. Chen, Q. Li, B.-B. Dong and C.-Y. Zhi, *Adv. Energy Mater.*, 2020, 2001024.